Received: 7 March 2025 | Revised: 27 August 2025 | Accepted: 2 September 2025

DOI: 10.1111/jace.70262

Journal of the American Ceramic Society

RESEARCH ARTICLE

Quantitative in situ studies of dynamic fracture in a lithium metasilicate glass-ceramic by x-ray phase contrast imaging

Liuchi Li[1] | **Arezoo Zare**[2] | **Xinyi Xu**[3] | **Velat Kilic**[4] | **Kevin Hom**[5] | **Laszlo Kecskes**[1] | **Samuel Clark**[6] | **Kamel Fezzaa**[6] | **Charlene Smith**[3] | **Jason Harris**[3] | **K. T. Ramesh**[1,5,7] | **Todd C. Hufnagel**[1,5,7]

[1]Hopkins Extreme Materials Institute, Johns Hopkins University, Baltimore, Maryland, USA

[2]School of Mechanical and Materials Engineering, Washington State University, Pullman, Washington, USA

[3]Corning Inc., Corning, New York, USA

[4]Department of Electrical and Computer Engineering, Johns Hopkins University, Baltimore, Maryland, USA

[5]Department of Materials Science and Engineering, Johns Hopkins University, Baltimore, Maryland, USA

[6]X-ray Science Division, Advanced Photon Source, Argonne National Laboratory, Lemont, Illinois, USA

[7]Department of Mechanical Engineering, Johns Hopkins University, Baltimore, Maryland, USA

Correspondence
K. T. Ramesh, Hopkins Extreme Materials Institute, Johns Hopkins University, Baltimore, MD 21218, USA.
Email: ramesh@jhu.edu;
Todd C. Hufnagel, Hopkins Extreme Materials Institute, Johns Hopkins University, Baltimore, MD 21218, USA.
Email: hufnagel@jhu.edu

Funding information
Corning Research and Development Corporation; Advanced Photon Source, Grant/Award Number: DE-AC02-06CH11357

Abstract

Glass-ceramics are produced through controlled crystallization of base glass, with many of their properties depending on the specific microstructures. With respect to their mechanical properties, although this dependence has been widely studied under quasi-static loading conditions, limited studies have been carried out beyond the quasi-static regime, especially in the context of fracture. Here, we study the fracture of lithium metasilicate glass-ceramics having different microstructures but nominally identical mechanical properties, under dynamic three-point-bend loading conditions. Using time-resolved x-ray phase contrast imaging, we capture crack initiation and propagation in glass-ceramics specimens and quantify the crack tip speed evolution. We find that the crack speed differs for specimens possessing different microstructures, an observation that cannot be captured by linear elastic fracture mechanics theory via a standard homogenization modeling procedure. Postmortem characterizations of fracture surfaces aided by scanning electron microscopy and white light interferometry reveal strong crack-crystal interactions (e.g., trans-granular fracture) and identify a correlation between a lower crack speed and an increased roughness of the fracture surface. Our work demonstrates microstructure-modulated fracture behavior in glass-ceramics and brings up the scale interplay between material heterogeneity and homogenization in the context of modeling fracture in heterogeneous materials.

KEYWORDS
dynamic fracture, glass-ceramics, material microstructure, x-ray phase contrast imaging

1 | INTRODUCTION

Glass-ceramics are produced through controlled partial crystallization of a base glass, and comprise one or more crystalline phases in an amorphous matrix. The ability to tailor the specific crystalline phases that form, together with their volume fraction(s) and crystallite size(s), enables the production of materials with advantageous combinations of properties for a wide range of applications.[1] Examples include a combination of transparency to visible light with fracture toughness for consumer electronics applications[2] and a combination of strength, toughness, and biocompatibility for dental implants and bone tissue engineering.[3]

In many applications, glass-ceramics are subjected to dynamic loading, due to which failure (such as crack propagation) may occur. The specific failure processes of an object depend on multiple factors including the loading condition, the geometry of the object, and the properties of the constituent materials. The loading condition and the object geometry may be constrained by the component design, making the material properties an important factor in determining overall performance. In glass-ceramics these properties are determined to a large extent by the microstructure, and indeed, both standard quasi-static mechanical characterization[4–7] and simulations (e.g., via molecular dynamics[8,9] or peridynamics[10]) suggest a strong dependence of failure behavior on microstructure.

However, most experimental investigations studying this dependence for glass-ceramics have been performed under quasi-static conditions, and studies under dynamic conditions are limited, particularly when compared to the extensive literature on glasses[11–14] and crystalline ceramics[15–20] separately. Most experimental studies of glass-ceramics to date consider either the effect of material microstructure under quasi-static loading[5,21] or look at dynamic loading without examining the effect of material microstructure.[22–24] Unlike quasi-static loading conditions, under dynamic loading conditions, a crack tip can experience considerable inertia effects such as wave interactions[25,26] as it propagates, and the underlying mechanics dictates its motion will be further complicated by the introduction of material heterogeneity via controlled crystallization and the accompanying thermal mismatch-induced residue stress.[27]

Here, we study the fracture of glass-ceramics specimens possessing nominally identical quasi-static mechanical properties (Young's modulus, Poisson's ratio, and fracture toughness) but with different microstructures. Using x-ray phase contrasting imaging (XPCI) to observe the propagating crack tip, we are able to isolate the effect of microstructure on the fracture process. XPCI exploits the phase perturbation introduced within a sample due to spatial variations in electron density to modulate the intensity recorded at the image detector plane.[28] Since a crack surface represents a steep electron density gradient, it can be detected with a significantly better sensitivity using XPCI than conventional radiography (which relies solely on absorption contrast). XPCI has been used to characterize the crack dynamics within different materials from ceramics[18] to glass.[29,30]

We show that the crack tip speed determined from the XPCI recordings depends sensitively on the microstructure of the glass-ceramic, even though the quasi-static mechanical properties of the materials (including the mode I fracture toughness) are identical. This is an observation which cannot be captured by linear elastic fracture mechanics theory via a standard homogenization modeling procedure. Postmortem analysis of the fracture surfaces reveals strong crack-crystal interactions (e.g., trans-granular fracture) and indicates that a rougher fracture surface is correlated with a slower crack. Our work reveals the importance of material microstructure and raises interesting questions regarding the scale interplay between material heterogeneity and homogenization treatment in the context of fracture modeling.

2 | EXPERIMENTAL PROCEDURE

2.1 | Sample preparation and preliminary characterization

We pick parent glasses in the multicomponent Li_2O-ZrO_2-K_2O-Al_2O_3-P_2O_5-SiO_2 glass family with Al_2O_3, varying the relative amounts of K_2O and Al_2O_3, because an increase in Al_2O_3 content is known to suppress lithium silicate crystallization, allowing some control over the crystallinity.[31,32] The compositions of all parent glasses are listed in Table 1. To produce the base glasses, precursor powders were melted in platinum crucibles at 1550 °C for 16 h in an electrical furnace and cast on a stainless steel table, followed by annealing at 450 °C for 1 h to relieve residual thermal stresses. The glasses produced in this way show no crystalline peaks in x-ray diffraction (XRD) patterns (not included here). To produce the glass-ceramics, we heat-treated the base glasses for 20 min at 750°C and furnace-cooled them to room temperature, resulting in opaque specimens. The goal of this procedure was to make glass-ceramics with a low volume fraction of relatively large (micron-scale) crystallites because we believed that this combination would give us the best chance to resolve interactions between the propagating cracks and the crystallites using XPCI. In actuality, the crystals were too small to be individually resolved, but we were still able to track the progression of the crack front during fracture, as described below.

The identities of the crystalline phases and their corresponding phase fractions were identified by XRD. Diffraction peaks were measured on powder samples over the range $2\theta = 10°–80°$, with a step size of 0.02° Cu K_α radiation. The major crystalline phase is lithium metasilicate (LMS; Li_2SiO_3), with a trace amount of lithium phosphate (LP; Li_3PO_4), as shown in Figure 1. Using a known amount

TABLE 1 Batch compositions of the parent glasses together with the mechanical properties (elastic modulus [E], shear modulus [G], Poisson's ratio [ν], and fracture toughness [K_Q]) of the corresponding glass-ceramics.

Glass							Glass-ceramics							
	Composition (mol.%)						Phase fraction (%)			Mechanical properties				
Li-Zr-K-Al-P-Si glass	SiO_2	Li_2O	Al_2O_3	K_2O	P_2O_5	ZrO_2	Glass	LMS	LP	E (GPa)	G (GPa)	ν	K_Q (MPa m$^{1/2}$)	σ_f (MPa)
First type (d_{20})	68.5	21	4	5	.5	1	82	17.8	.2	84.46	35.23	0.198	1.36 ± 0.07	330 ± 33
Second type (d_{10})	68.5	21	5	4	.5	1	82	17.4	.6	84.25	35.3	.193	1.35 ± 0.04	265 ± 47
Third type (d_5)	68.5	21	6	3	.5	1	88	10.3	.7	82.32	34.54	.19	1.31 ± .03	260 ± 41

Abbreviations: LMS, lithium metasilicate; LP, lithium phosphate

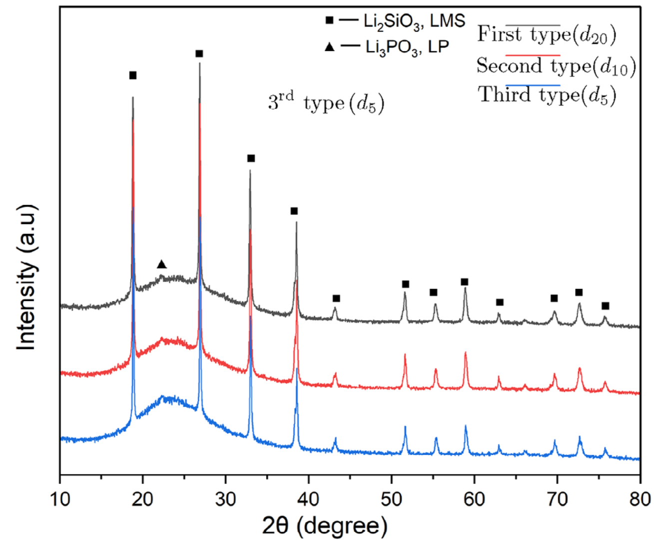

FIGURE 1 X-ray diffraction (XRD) patterns of glass ceramic samples of the compositions listed in Table 1.

of α-alumina added to the powdered glass-ceramics as an external reference, crystalline phase fractions were estimated by Rietveld refinement and are reported in Table 1. A similar level crystallinity of 18% was obtained for the first type d_{20} (17.8% LMS plus .2% LP) and the second type d_{10} (17.4% LMS plus .6% LP) specimens, with a slightly lower value of 12% (11.3% LMS plus .7% LP) for the third type.

The microstructures of the samples were examined by scanning electron microscopy (SEM). All the SEM observations required a careful cleaning procedure to remove electrostatically adhering contaminants and stains from the sample surfaces. This entailed washing the samples in a soapy solution, followed by an acetone and an alcohol rinse, and finally by air drying using a heat source. The dendrite-like crystals shown in Figure 2 are characteristic of LMS,[4,31,33,34] confirming therefore their presence in glass-ceramics of the multicomponent series. For the sake of convenience and clarity, hereafter we refer the first type of glass-ceramic as d_{20}, the second type as d_{10}, and the third type as d_5. Here, d indicates the largest dimension of the crystal and the subscript number indicates the corresponding value with a micrometer unit. These values are rough estimations based on the SEM scans shown in Figure 2.

The mechanical properties of our samples are summarized in Table 1. The elastic modulus (E), shear modulus (G), and Poisson's ratio (ν) of the glass-ceramics were measured from 6 mm × 8 mm × 10 mm specimens via resonant ultrasound spectroscopy. The apparent fracture toughness (K_Q) was measured using chevron-notch short bar specimens following the protocol described in ASTM E1304-97. The fracture toughnesses of the three microstructures are measured to be similar.

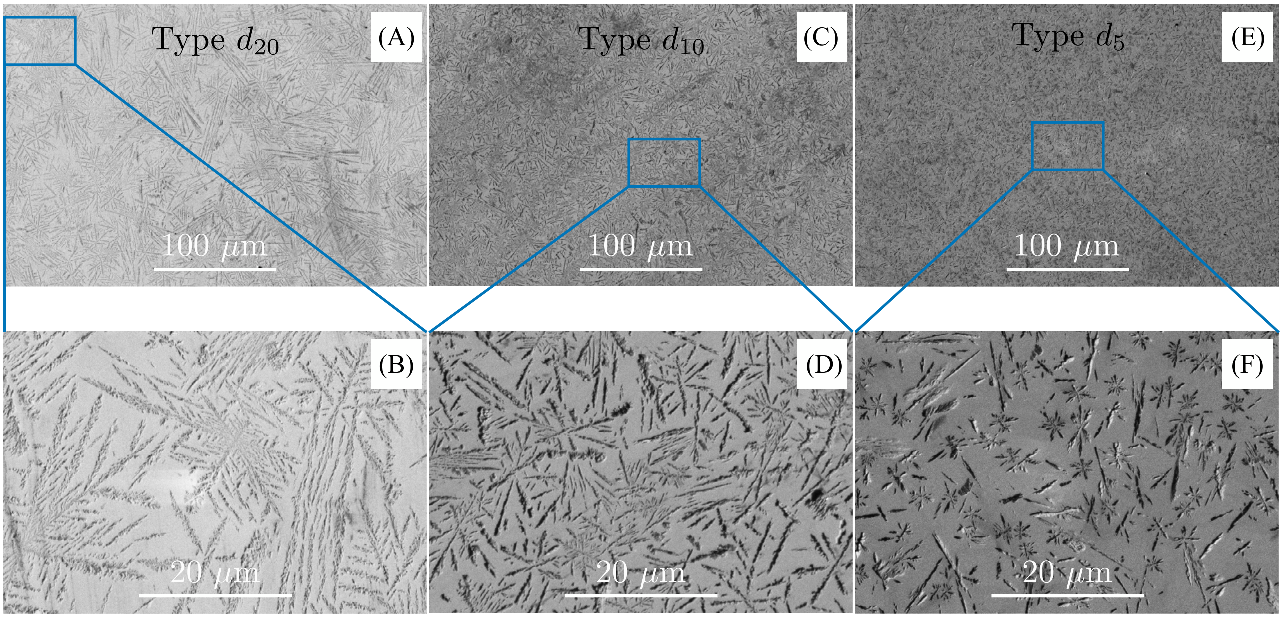

FIGURE 2 Scanning electron microscopy (SEM) micrographs of the microstructure for glass-ceramics specimens of Type d_{20} (A and B), Type d_{10} (C and D), and Type d_5 (E and F).

We also measured the flexural strength, σ_f, of these specimens. To do so, 20 samples of each composition were cut into rectangular specimens (12 mm × 3 mm × 1.5 mm) and loaded in three-point bending with a span between rollers of L =9 mm and a crosshead speed of 5 mm/min. Based on the load at failure (P) and the specimen geometry (specimen width w and thickness b), the flexural strength values were calculated using

$$\sigma_f = \frac{3PL}{2wb^2}. \tag{2.1}$$

Interestingly, although the elastic properties and fracture toughness of the three materials are virtually identical, the flexural strength of the Type d_{20} specimens was significantly higher than that of Types d_{10} and d_5.

2.2 | In situ x-ray imaging and dynamic three-point bending

We conducted in situ x-ray phase contrast imaging (XPCI) studies during dynamic notched three-point bending of glass-ceramics samples at Sector 32 of the Advanced Photon Source (APS) at Argonne National Laboratory. Samples for the in situ XPCI studies were of the same size as those used to measure flexural strength. For XPCI the broad surfaces were polished to a mirror finish to minimize the influence of surface roughness on XPCI image formation, and a notch (nominally 1 mm deep) was made in the center of one long side to create a stress concentration at which cracks would initiate. We used the unfiltered first harmonic of the U18 undulator (with a gap distance of 12 mm) providing an x-ray spectrum with a peak intensity at around 24 keV and an energy bandpass of approximately 3% − 4%. For dynamic imaging the x-rays are converted into visible light via a 100 μm thick single-crystal $Lu_3Al_5O_{12}$: Ce scintillator, then focused onto a 250×400 pixel Shimadzu HPV-X2 camera using a 10x infinity-corrected objective lens, yielding an effective pixel size of about 3 μm. Propagation-based XPCI was produced with a sample-to-scintillator distance of 308 mm, chosen to achieve both good contrast ratio and sufficient spatial resolution of the cracks without saturating the camera. The field of view of the specimen is about .75 mm in the horizontal direction and 1.2 mm in the vertical direction (which is also the crack propagation direction). During our experiments, the APS storage ring was operating in the standard 24-bunch fill mode, which produces one pulse of x-rays every 153.4 ns. Refer to Leong et al.[18] for more detailed information on the imaging setup, including the procedure for synchronizing the camera framing with the synchrotron x-ray pulses.

The notched three-point bend specimens were loaded to fracture using a custom-built apparatus. The samples were placed on two rolling supports on a loading plate sitting atop a vertical translation stage (OptoSigma TSD-653DMUU). The central roller (on the top side of the specimen) was driven by a piezoelectric actuator (Cedrat Technologies PPA40M), with the actuator being driven by a voltage signal that is generated by a function generator (Tektronix AFG3252) and then amplified by a high-speed voltage amplifier (PiezoDrive PD200). We use the function

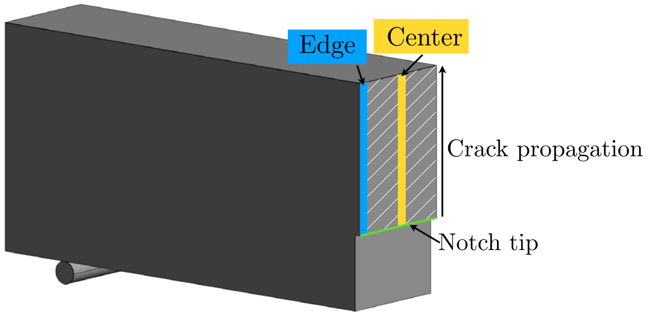

FIGURE 3 Schematic representation of the two locations where the surface roughness is estimated: along the edge (blue strip) and the center (yellow strip).

generator to output a linear voltage ramp from 0 V to 7 V over an interval of 256 μs, from which the displacement rate is calculated to be about .13 m/s. Additional details of this setup, as well as the calculation procedure of the displacement rate, are provided in Li et al.[35]

2.3 | Fractography

To gain insights into the underlying fracture mechanisms and the corresponding effects of microstructure, we characterized the fracture surfaces of different glass-ceramic specimens both qualitatively and quantitatively. A Thermo Scientific Helios G4 UC dual-beam SEM was used to compare the topography of the fractured surfaces qualitatively and study possible crack-crystal interactions. A Filmetrics Profilm3D optical profilometer was also used to measure the average surface roughness (R_a), including its evolution along the crack propagation path. The roughness was measured on both the edge and center of the fractured surface, as shown in Figure 3. Both SEM and optical profilometry were performed directly on the fractured surfaces (without any polishing or coating) after cleaning using the same procedure described above.

3 | XPCI OBSERVATIONS OF DYNAMIC FRACTURE IN GLASS-CERAMICS

Figure 4 shows selected frames from representative XPCI recordings of crack propagation in each of the three types of glass ceramic. The left-most image in each row, arbitrarily set as time $t = 0$, is the frame immediately prior to the frame in which the crack was first detected (in the next column to the right). Because the frame rate of the camera was 5 Mfps, the minimum time between frames is 0.2 μs. We note, though, that the sample is imaged at times determined by the x-ray pulses, which occur every 0.153 μs. We have taken this into account in our image analysis following the procedure described in Ref. [18].

It can be observed that a crack initiates at one of the corners of the notch tip due to stress concentration there. The specific location of crack initiation likely depends on the defects introduced by notching the specimen. An advantage of XPCI for studying crack propagation in opaque specimens is that we can see the entire crack front, in projection through the specimen. In Figure 4B, the fracture surface is nearly parallel to the direction of propagation of the x-rays and hence appears as an essentially linear feature. In Figure 4A,C, on the other hand, the fracture surface is inclined to the direction of view, but we can identify the portion of the crack front that has advanced furthest (white triangle in the images). From multiple runs (see Figures A.1–A.3 for additional XPCI recordings), we note that, however, the fracture surface can be parallel or inclined with respect to the direction of the x-ray beam, regardless of the type of glass ceramic tested. Assuming that the fracture surface is planar on the length scale of the sample's thickness, we estimate from the XPCI recordings that its angle of inclination (with respect to the direction of the x-ray beam) is less than 10°. This inclination could be induced by a less ideal alignment between the sample's notch and the indenter.

Regardless, we observe that once a crack initiates it propagates rapidly through the sample, leaving the field of view in about one µs. From the crack tip locations in each frame, we can estimate the instantaneous crack tip speed. The uncertainty associated with crack tip speed was based on the uncertainty of the crack tip location (estimated to be about 14 μm[18]). As also discussed in Leong et al.[18], there is another source of uncertainty for crack tip location, which is associated with the formation of far-field diffraction (rather than near-field phase contrast) pattern in x-ray images due to atomic-scale crack surface opening.[37] As a result, the true crack tip location is some small but unknown distance ahead of the location identified in the XPCI images. Nevertheless, it is not essential to quantify this discrepancy; it is expected to remain constant because the crack speed is calculated from the difference in crack tip location across frames.

After identifying crack tip locations from XPCI images, we can estimate the instantaneous crack tip speed as a function of time. Figure 5A shows the instantaneous crack velocity as a function of the distance of the crack tip back to the crack initiation location. Each color corresponds to one of the three types of glass ceramic (d_{20}, d_{10}, or d_5), and each symbol corresponds to results obtained from one experiment. We observe a general trend that is consistent across all three types of material microstructure: Once a crack initiates, its velocity first increases and decreases quickly afterward.

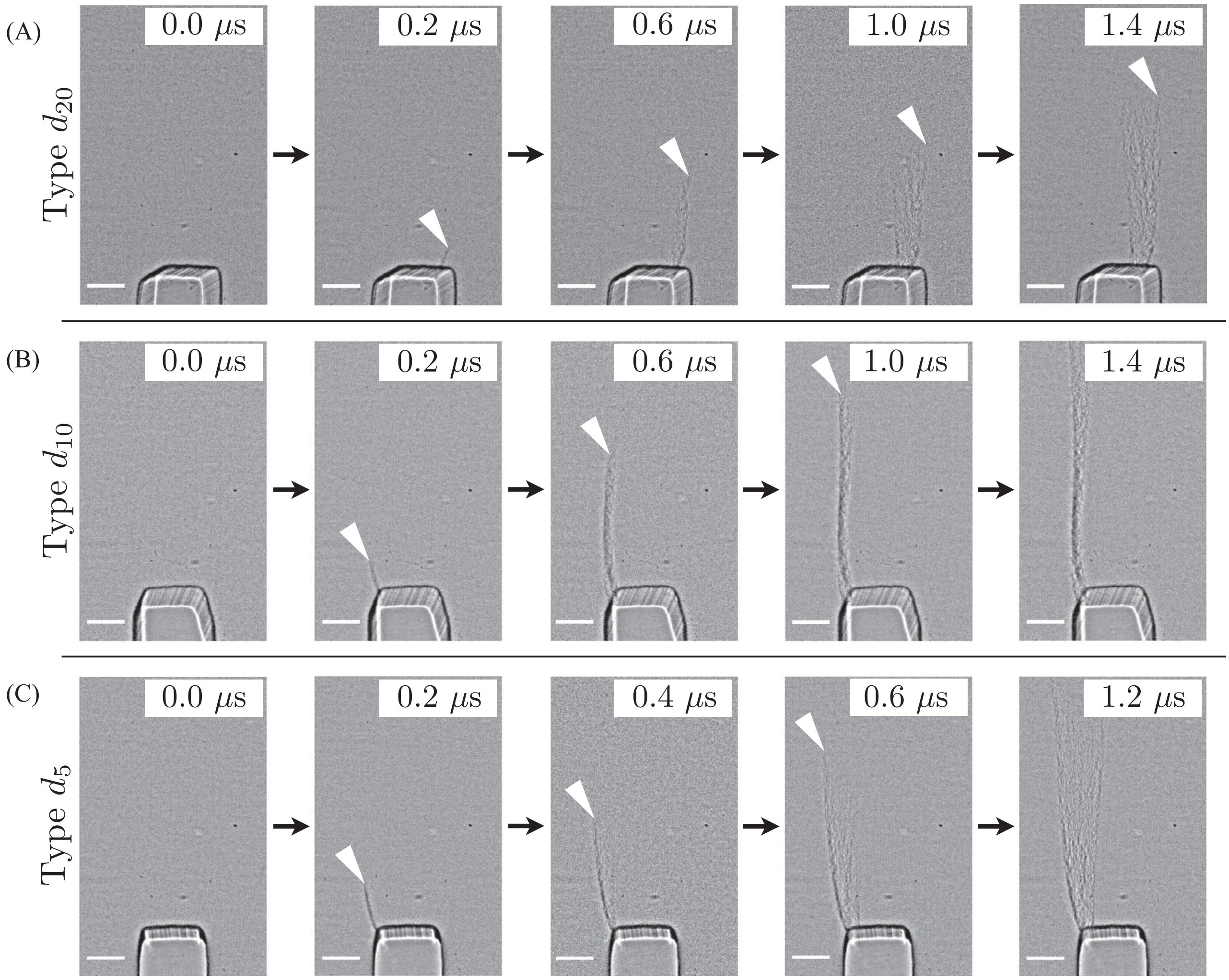

FIGURE 4 Representative x-ray phase contrast imaging (XPCI) recordings of crack propagation in three specimens, each of which corresponds to a particular microstructure: Type d_{20} (A), Type d_{10} (B), and Type d_5 (C). For each, the frame in the left-hand column is the last frame prior to observation of the propagating crack, and the next frame to the right is the subsequent frame. The scale bar is .2 mm for all images. The white triangles indicate the location of the crack tip at different times. Note that these images have been post-processed from raw XPCI frames via the "enhance contrast" option in ImageJ,[36] to aid in identifying the location of the crack tip.

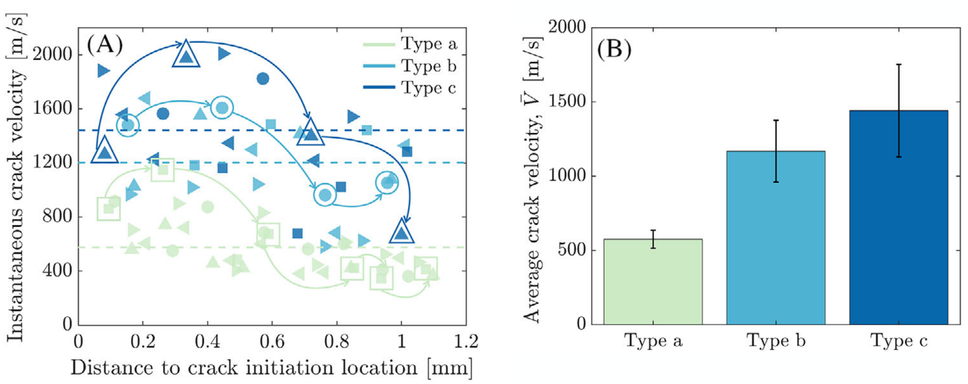

FIGURE 5 Crack tip velocities from x-ray phase contrast imaging (XPCI) observations. (A) Instantaneous crack velocity as a function of the distance to crack initiation location. Samples of each microstructure (A, B, or C) are indicated by the same color, with individual specimens distinguished by the symbol shape. The frame-to-frame progression of one specimen of each type is indicated by the arrows. The dashed lines represent the average velocity for each type of specimen. (B) Time-average crack velocity calculated from the XPCI data in (A), along with the standard deviation.

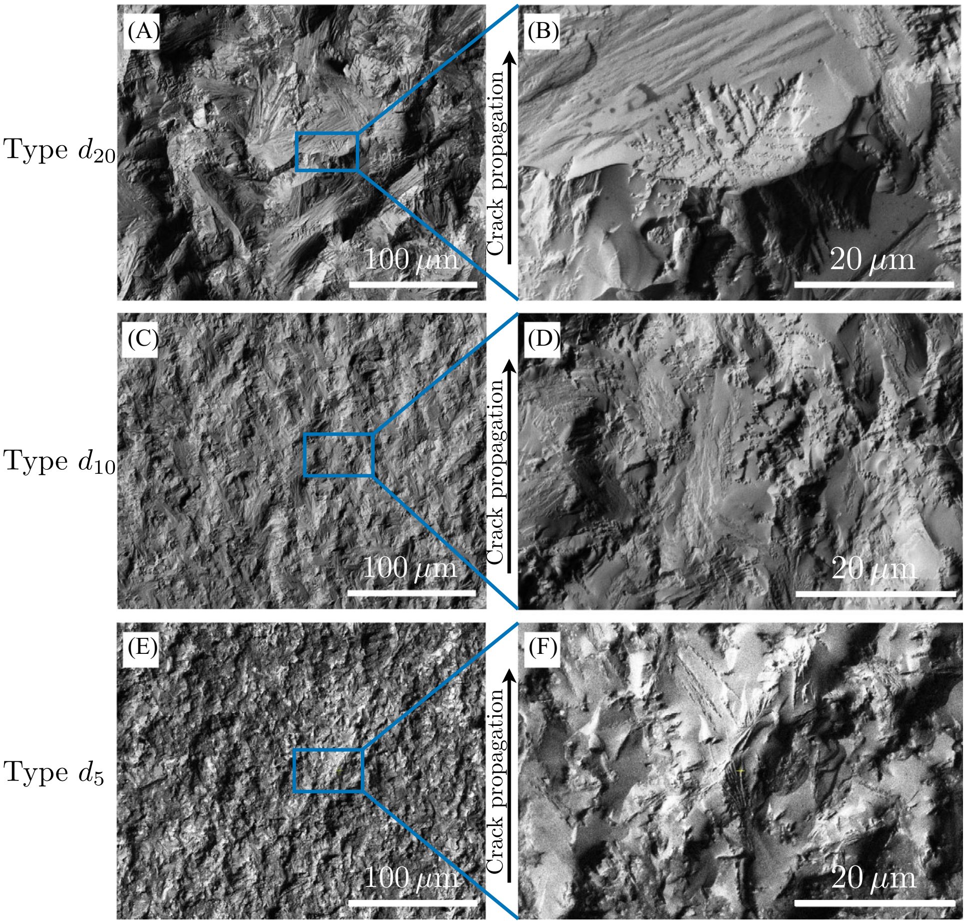

FIGURE 6 (A) A scanning electron microscopy (SEM) image of the fracture surface for a glass-ceramic specimen with Type d_{20} microstructure. (B) A zoomed-in image of (a) highlighting the crack-crystal interaction. Subparts (C and D) and (E and F) correspond to SEM images of a glass-ceramic specimen with Type d_{10} and Type d_5 microstructure, respectively.

As a first-order description of the crack speed, Figure 5B quantifies the time-averaged crack speed from XPCI analysis, which gives $\bar{V}_a = 637.8$ m/s $< \bar{V}_b = 1168.4$ m/s $\simeq \bar{V}_c = 1421.5$ m/s. The observed difference in crack velocity suggests the potential role of material microstructure in modulating crack speed, which we discuss in the next section via postmortem analysis.

4 | ANALYSIS OF FRACTURE SURFACES

The difference in crack speed between the Type d_{20} microstructure and the other two may be due to crack-crystal interactions (such as crack deflection by crystals). The specific material microstructure (e.g., crystal size and spacing) can be important in determining these interactions. To examine such interactions and the role of material microstructure, we conducted postmortem analysis of the fracture surfaces to gain insights into the mechanisms at play during crack propagation.[38,39]

Figure 6 shows SEM micrographs obtained from the fractured surfaces of the three types of glass-ceramic microstructures. Qualitatively, it is observed that the fractured surface of Type d_{20} (Figure 6A,B) has a more pronounced texture compared to Type d_{10} (Figure 6C,D) and Type d_5 (Figure 6E,F), which correlates well with the observation that the crystal size for Type d_{20} is on average larger than that for Type d_{10} and Type d_5 (see Figure 2). The crack-crystal interactions for Type d_{20} also appear to be more pronounced compared to the other two types of microstructures. An example of such interactions is shown in Figure 6B where the crack is seen to deflect while passing through a dendritic crystal and results in a "ridge" on the fracture surface: A part of that crystal is on one plane and a part is on another plane.

Figure 7 shows the average surface roughness of the fractured surfaces quantified using optical profilometry. We note Type d_{20} shows the largest average roughness value (about 1.2 μm), while types B and C have similar roughness (about .6 μm on average). There is no significant variation in roughness along the crack propagation

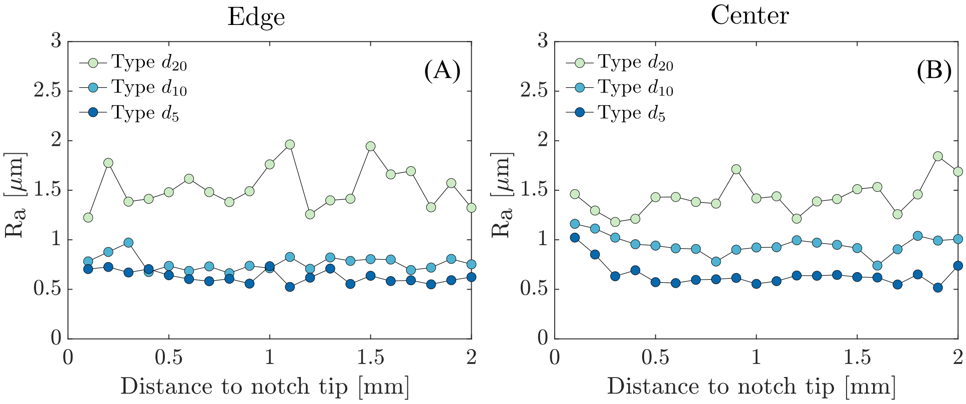

FIGURE 7 Variation of surface roughness as a function of the distance to the notch tip for all three types of material microstructures, determined via optical profilometry, measured along the edge (A) and the center (B) of each fracture surface (refer back to Figure 3).

direction, and no difference between roughness along the centerline of the sample compared to the near-surface region (refer back to Figure 3).

5 | DISCUSSION

The three types of glass-ceramic microstructures examined here are nearly identical with regard to their elastic properties and plane-strain fracture toughness but show differences in both flexural strength and crack-tip velocity under dynamic loading (Table 1; Figure 5). Specifically, the Type d_{20} microstructure shows both the highest flexural strength and the lowest crack-tip velocity. These differences in mechanical behavior correlate with the roughness of the fracture surfaces, with Type d_{20} having the roughest. From Figure 2 we also see that the Type d_{20} microstructure has the largest crystals and relatively large regions without crystals. (This is most apparent in the low-magnification views in parts a, c, and e of the figure.) These observations suggest that the differences in behavior are associated with the interaction between the propagating crack tip and the material microstructure. Specifically, it appears that the coarser microstructure in the Type d_{20} specimens leads to greater crack deflection during fracture.

Serbena and coworkers evaluated the relative importance of several mechanisms including crack deflection, crack bowing/trapping, and crack bridging on the fracture behavior of lithium disilicate glass-ceramics, varying the crystalline volume fraction while maintaining a constant crystallite size (of about 12 μm[5]). For low volume fractions of crystallites, comparable to those studied here, they concluded that the primary contributions to toughening were crack bowing and trapping, with crack deflection playing only a minor role. On the other hand, Prakash and coworkers concluded (from peridynamics simulations of crack growth) that crack deflection is a major contributor to toughness at low volume fractions.[10]

Inspection of the fracture surfaces in Figure 6 and the quantitative roughness measurements in Figure 7 do suggest to us that some crack deflection occurs. However, the interaction between the crack and crystallites is complex. In some cases the crack appears to propagate along the crystal/glass interface, leaving behind a dendrite-shaped impression on the fracture surface (Figure 6B). In other cases, the crack propagates through the dendrite itself (not shown). Crack bridging by dendrites appears not to be important, partly due to the low volume fraction of the crystalline phase, and also because the LMS dendrites appear to have a planar (2D) morphology, making it easier for the crack to bypass them without bridging in the crack-tip wake. We note that planar dendrites of LMS have been observed during growth by solid-state reaction,[34] but we are unaware of any detailed characterization of dendrites produced by devitrification.

Finally, although the physics of precisely why the cracks behave as they do is not yet resolved, our results also raise interesting questions regarding the influence of length scales on the modeling of fracture problems in heterogeneous solids. The samples studied here have slightly different compositions and volume fractions of crystallites, but their macroscopic mechanical properties are nearly identical. On this basis we hypothesized that the microstructure of the material would have no effect on the crack speed estimated from a simple continuum mechanics model (such as a phase-field model[40]) that uses these macroscopic mechanical properties. However, the length scale at which mechanical properties or behaviors are sampled matters. If the region sampled is large relative to the characteristic length scale of the microstructure, then the measurements will reveal average properties with little variation. As the size of the sampled region is reduced, variations in properties will emerge due to statistical variation in the microstructure (and indeed we do see variations among the limited number of samples studied here). In the limit, details of the specific local microstructure (such as the sizes and distributions of the crystallites) dominate. Understanding crack dynamics in this regime clearly requires explicit consideration of the microstructure. This can be done computationally (by phase field or cohesive zone simulations[41–43]) or experimentally, but such detailed studies are typically complicated and expensive. We propose that there may be an intermediate scale at which the measured mechanical properties reflect the effect of material microstructure on crack propagation in a time-averaged sense, but which is not so small that explicitly modeling the material microstructure is necessary.[42] The ability to determine this length scale could be valuable for computational modeling of fracture, balancing the need to account for the influence of microstructure with the need for computational efficiency.

6 | SUMMARY

Through a combination of in situ XPCI and postmortem analysis, we identify the importance of microstructure in affecting dynamic crack propagation in glass-ceramics. In particular, postmortem analysis of the fracture surface reveals noticeable crystal-crack interactions, resulting in different levels of surface roughness with larger crystal size correlating to larger surface roughness and lower crack speed. This difference is not, however, represented in the fracture toughness measured under conditions of stable crack growth in standard (quasi-static) tests. Furthermore, because the macroscopic elastic properties of the materials studied here are nearly identical, the differences in behavior that we observe would not be captured in continuum models of dynamic crack propagation. This highlights the importance of measuring variations in mechanical properties on an appropriate length scale, to be used as inputs to computational models of crack growth.

ACKNOWLEDGMENTS

We thank Elena Bronder-Chang, Ronald Agyei, Brett Kuwik, and Alex Deriy for their assistance with the experiments conducted at APS, Ryan Hurley for providing access to the WLI profilometer in his lab, as well as Andrew FT Leong for helping with XPCI image analysis. We gratefully acknowledge financial support provided by the Corning Research and Development Corporation. This research used resources of the Advanced Photon Source, a DOE Office of Science User Facility operated for the DOE Office of Science by Argonne National Laboratory under Contract No. DE-AC02-06CH11357. This work was conducted at Hopkins Extreme Materials Institute, Johns Hopkins University, Baltimore, MD.

CONFLICT OF INTEREST STATEMENT

This research was funded by Corning, Inc. through a contract to Todd C. Hufnagel and K. T. Ramesh. Xinyi Xu, Charlene Smith, and Jason Harris are employees of Corning Inc.

DATA AVAILABILITY STATEMENT

Data will be made available upon request.

ORCID

Liuchi Li https://orcid.org/0000-0002-1360-4757
Todd C. Hufnagel https://orcid.org/0000-0002-6373-9377

REFERENCES

1. Zanotto ED. A bright future for glass-ceramics. Am Ceram Soc Bull. 2010;89(8):19–27.
2. Beall G, Pinckney L. Nanophase glass-ceramics. J Am Ceram Soc. 1999;82(1):5–16.
3. Hoppe A, Gueldal NS, Boccaccini AR. A review of the biological response to ionic dissolution products from bioactive glasses and glass-ceramics. Biomaterials. 2011;32(11):2757–74.
4. Fernandes HR, Tulyaganov DU, Ferreira JM. The role of P_2O_5, TiO_2 and ZrO_2 as nucleating agents on microstructure and crystallization behaviour of lithium disilicate-based glass. J Mater Sci. 2013;48:765–73.
5. Serbena F, Mathias I, Foerster C, Zanotto E. Crystallization toughening of a model glass-ceramic. Acta Mater. 2015;86:216–28.
6. Hallmann L, Ulmer P, Kern M. Effect of microstructure on the mechanical properties of lithium disilicate glass-ceramics. J Mech Behav Biomed Mater. 2018;82:355–70.
7. Kim D, Kim HJ, Yoo SI. Effects of microstructures on the mechanical properties of lithium disilicate glass-ceramics for the SiO_2–Li_2O–P_2O_5–K_2O–ZnO system. Mater Sci Eng, A. 2021;804:140564.
8. Urata S, Takato Y, Maeda K. Molecular dynamics investigation of the fracture mechanism of a glass-ceramic containing cleavable crystals. J Am Ceram Soc. 2019;102(9):5138–48.
9. Deng B, Harris JT, Luo J. Atomic picture of crack propagation in Li_2O-$2SiO_2$ glass-ceramics revealed by molecular dynamics simulations. J Am Ceram Soc. 2020;103(8):4304–12.
10. Prakash N, Deng B, Stewart RJ, Smith CM, Harris JT. Investigation of microscale fracture mechanisms in glass–ceramics using peridynamics simulations. J Am Ceram Soc. 2022;105(6):4304–20.
11. Nie X, Chen WW, Sun X, Templeton DW. Dynamic failure of borosilicate glass under compression/shear loading experiments. J Am Ceram Soc. 2007;90(8):2556–62.
12. Park H, Chen WW. Experimental investigation on dynamic crack propagating perpendicularly through interface in glass. J Appl Mech. 2011;78:051013.
13. Sundaram BM, Tippur HV. Dynamic fracture of soda-lime glass: a full-field optical investigation of crack initiation, propagation and branching. J Mech Phys Solids. 2018;120:132–53.

14. Dondeti S, Tippur H. Cascading crack bifurcations in soda-lime glass: Quantification of fracture mechanics-based precursors using digital gradient sensing. Int J Solids Struct. 2022;234:111252.
15. Suresh S, Nakamura T, Yeshurun Y, Yang KH, Duffy J. Tensile fracture toughness of ceramic materials: effects of dynamic loading and elevated temperatures. J Am Ceram Soc. 1990;73(8):2457–66.
16. Chen WW, Rajendran A, Song B, Nie X. Dynamic fracture of ceramics in armor applications. J Am Ceram Soc. 2007;90(4):1005–18.
17. Hogan JD, Farbaniec L, Shaeffer M, Ramesh K. The effects of microstructure and confinement on the compressive fragmentation of an advanced ceramic. J Am Ceram Soc. 2015;98(3):902–12.
18. Leong AF, Robinson AK, Fezzaa K, Sun T, Sinclair N, Casem DT, et al. Quantitative in situ studies of dynamic fracture in brittle solids using dynamic x-ray phase contrast imaging. Exp Mech. 2018;58:1423–37.
19. Wang Z, Li R, Song W. Dynamic failure and inelastic deformation behavior of SiC ceramic under uniaxial compression. Ceram Int. 2020;46(1):612–17.
20. Zare A, Malhotra P, Yang Q, Christian K, Du J, Haber RA, et al. The effects of carbonaceous inclusions and their distributions on dynamic failure processes in boron carbide ceramics. J Am Ceram Soc. 2023;106(8):4831–51.
21. Apel E, Deubener J, Bernard A, M Höland, R Müller, H Kappert, et al. Phenomena and mechanisms of crack propagation in glass-ceramics. J Mech Behav Biomed Mater. 2008;1(4):313–25.
22. Chen W, Ravichandran G. Dynamic compressive failure of a glass ceramic under lateral confinement. J Mech Phys Solids. 1997;45(8):1303–28.
23. Dong S, Xia K, Huang S, Yin T. Rate dependence of the tensile and flexural strengths of glass–ceramic Macor. J Mater Sci. 2011;46:394–99.
24. Zhang L, Townsend D, Petrinic N, Pellegrino A. Loading mode and lateral confinement dependent dynamic fracture of a glass ceramic macor. J Dynam Behav Mater. 2022;8(2):255–72.
25. Ravi-Chandar K, Knauss WG. An experimental investigation into dynamic fracture: IV. On the interaction of stress waves with propagating cracks. Int J Fract. 1984;26:189–200.
26. Goldman T, Livne A, Fineberg J. Acquisition of inertia by a moving crack. Phys Rev Lett. 2010;104(11):114301.
27. Borom MP, Johnson CA. Thermomechanical mismatch in ceramic-fiber-reinforced glass-ceramic composites. J Am Ceram Soc. 1987;70(1):1–8.
28. Endrizzi M. X-ray phase-contrast imaging. Nucl Instrum Methods Phys Res A.ectors and. 2018;878:88–98.
29. Parab ND, Black JT, Claus B, Hudspeth M, Sun J, Fezzaa K, et al. Observation of crack propagation in glass using x-ray phase contrast imaging. Int J Appl Glass Sci. 2014;5(4):363–73.
30. Kang M, Li W, Leong A, Guan M, Fezzaa K, Harris JT, et al. Crack nucleation and growth during dynamic indentation of chemically-strengthened glass. Extreme Mech Lett. 2020;38:100754.
31. Simba BG, Ribeiro MV, Suzuki PA, Alves MFR, Strecker K, Dos Santos C. Mechanical properties of lithium metasilicate after short-term thermal treatments. J Mech Behav Biomed Mater. 2019;98:179–86.
32. Kolay S, Bhargava P. Effect of $K_2O:Al_2O_3$ ratio on crystallization phenomena and microstructure of lithium silicate glass-ceramics. Trans Indian Ceram Soc. 2021;80(4):242–50.
33. Zhang H, He Z, Zhang Y, Jing W, Wang B, Yang J. Lithium disilicate glass-ceramics by heat treatment of lithium metasilicate glass-ceramics obtained by hot pressing. J Am Ceram Soc. 2015;98(12):3659–62.
34. Córdoba JM, Ballem MA, Johansson EM, Odén M. Growth of single crystalline dendritic Li_2SiO_3 arrays from $LiNO_3$ and mesoporous SiO_2. J Solid State Chem. 2011;184(7):1735–39.
35. Li L, Kilic V, Alemohammad M, Yang L, Ramesh KT, Foster MA, et al. Shack–Hartmann wavefront sensing: A new approach to time-resolved measurement of the stress intensity factor during dynamic fracture. Mech Mater. 2024;194:105010.
36. Schneider CA, Rasband WS, Eliceiri KW. NIH Image to ImageJ: 25 years of image analysis. Nat Methods. 2012;9(7):671–75.
37. Gureyev TE, Nesterets YI, Stevenson AW, Miller PR, Pogany A, Wilkins SW. Some simple rules for contrast, signal-to-noise and resolution in in-line x-ray phase-contrast imaging. Opt Express. 2008;16(5):3223–41.
38. Bonamy D, Ponson L, Prades S, Bouchaud E, Guillot C. Scaling exponents for fracture surfaces in homogeneous glass and glassy ceramics. Phys Rev Lett. 2006;97(13):135504.
39. Ponson L, Auradou H, Pessel M, Lazarus V, Hulin JP. Failure mechanisms and surface roughness statistics of fractured Fontainebleau sandstone. Phys Rev E. 2007;76(3):036108.
40. Borden MJ, Verhoosel CV, Scott MA, Hughes TJ, Landis CM. A phase-field description of dynamic brittle fracture. Comput Meth Appl Mech Eng. 2012;217:77–95.
41. Wu JY, Huang Y, Nguyen VP. On the BFGS monolithic algorithm for the unified phase field damage theory. Comput Meth Appl Mech Eng. 2020;360:112704.
42. Li L, Rao J, Hufnagel TC, Ramesh K. Meso-scale size effects of material heterogeneities on crack propagation in brittle solids: Perspectives from phase-field simulations. Int J Solids Struct. 2024;296:112795.
43. Rezaei S, Mianroodi JR, Brepols T, Reese S. Direction-dependent fracture in solids: Atomistically calibrated phase-field and cohesive zone model. J Mech Phys Solids. 2021;147:104253.

How to cite this article: Li L, Zare A, Xu X, et al. Quantitative in situ studies of dynamic fracture in a lithium metasilicate glass-ceramic by x-ray phase contrast imaging. J Am Ceram Soc. 2025;e70262. https://doi.org/10.1111/jace.70262

APPENDIX A: ADDITIONAL XPCI RECORDINGS

We provide in Figures A.1–A.3 additional XPCI recordings for the three types of glass ceramic considered in this work.

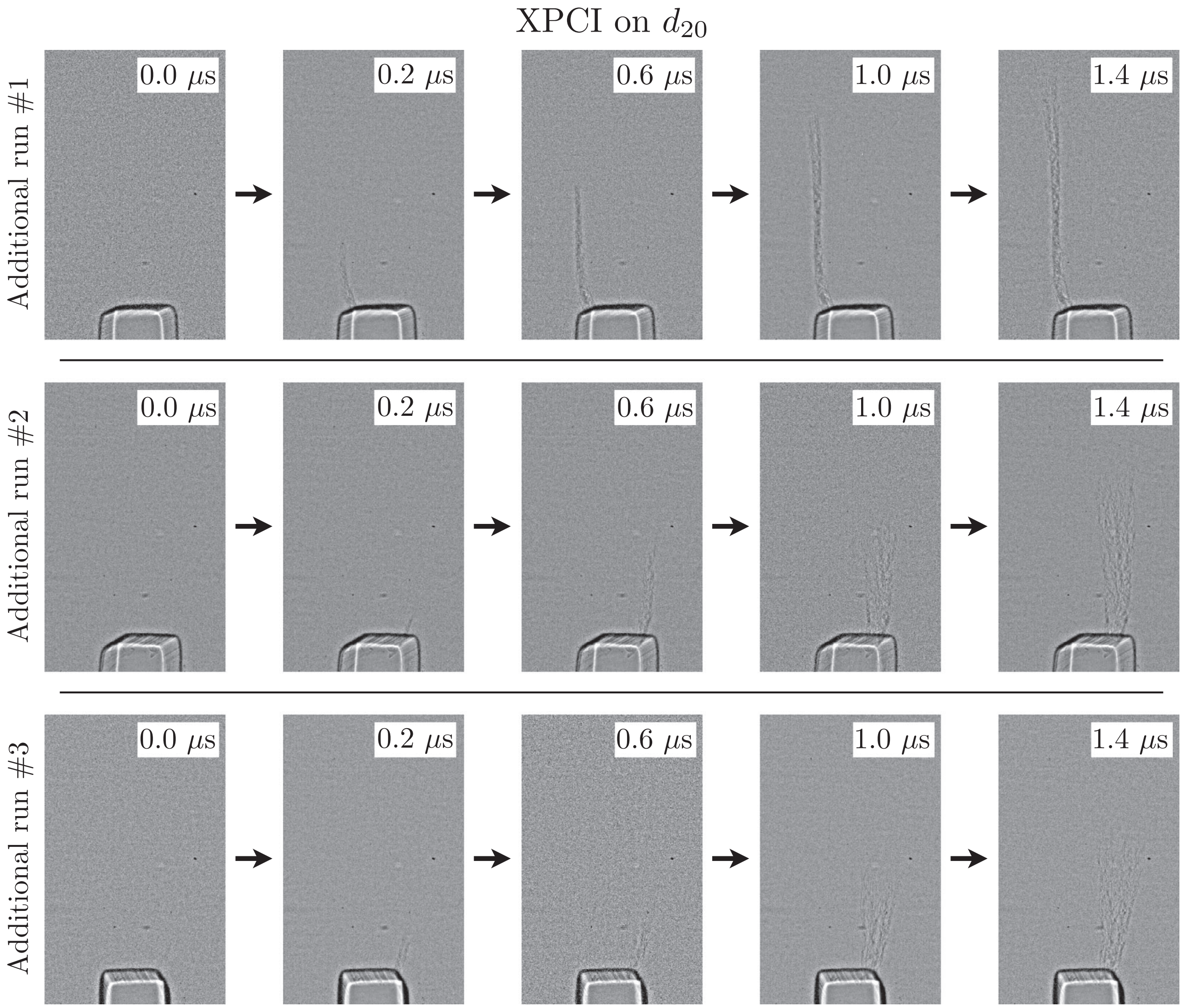

FIGURE A.1 Three additional experiments performed on d_{20} with x-ray phase contrast imaging (XPCI).

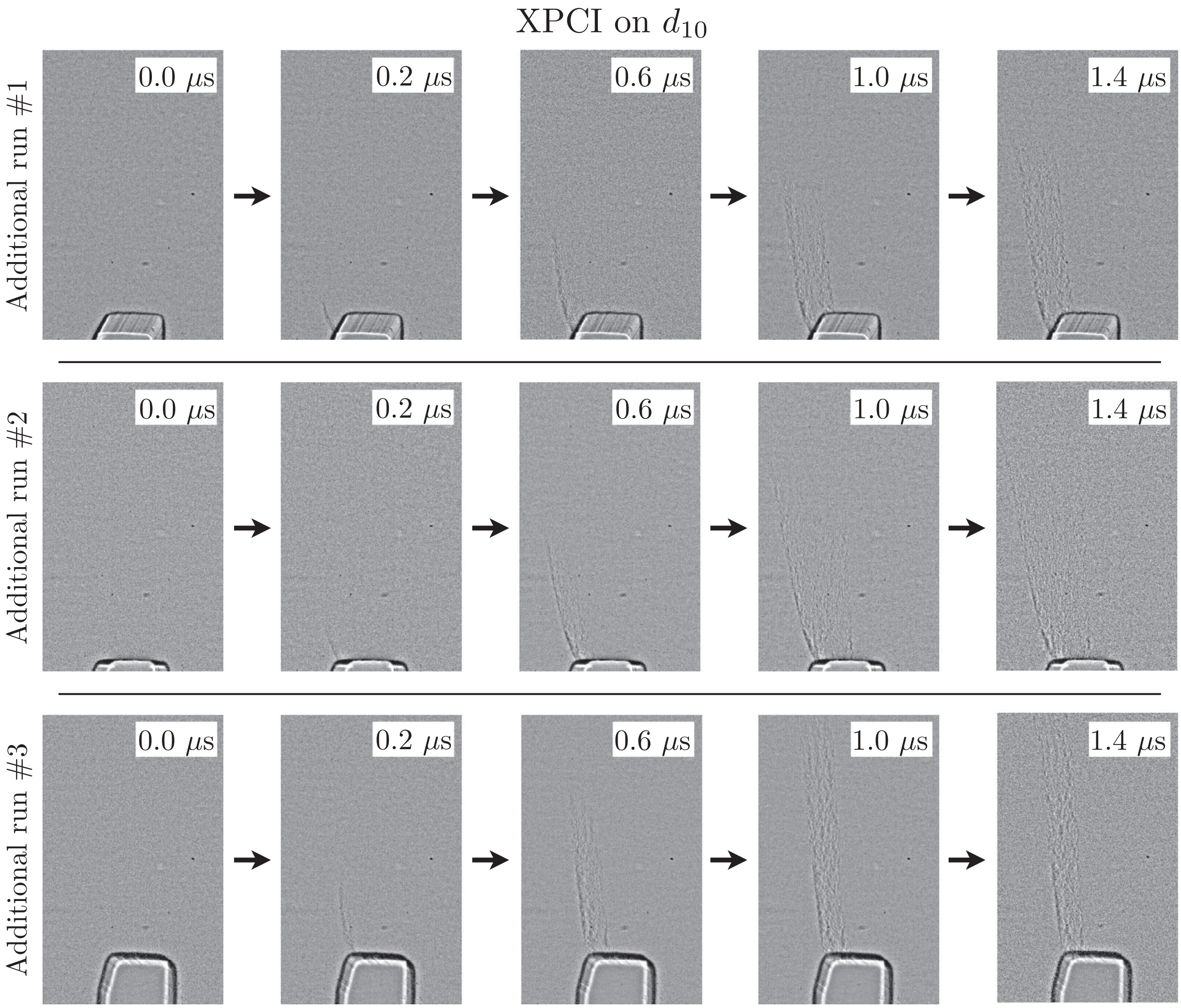

FIGURE A.2 Three additional experiments performed on d_{10} with x-ray phase contrast imaging (XPCI).

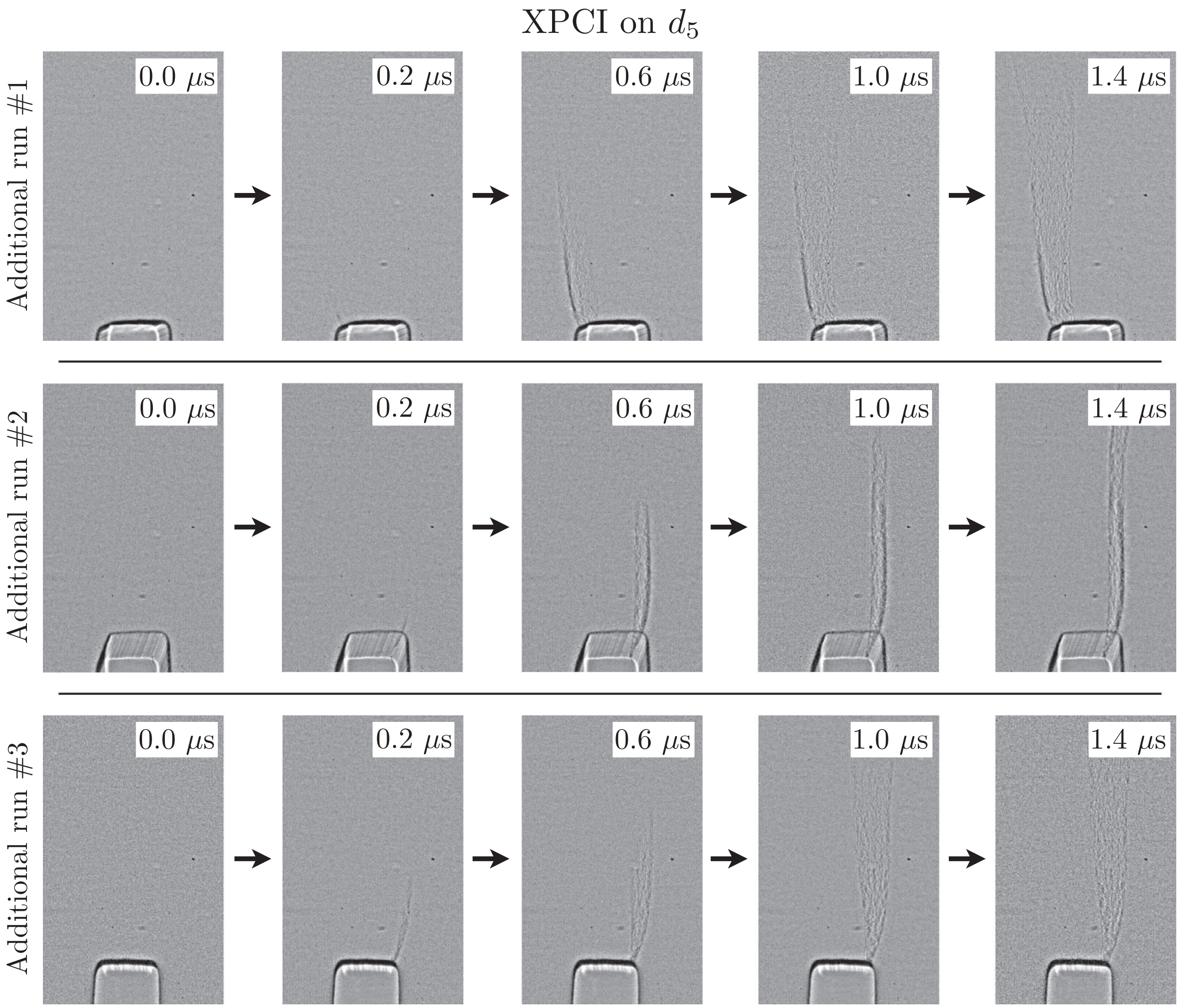

FIGURE A.3 Three additional experiments performed on d_5 with x-ray phase contrast imaging (XPCI).